Mehdi Farsad
Department of Mechanical Engineering,
Michigan State University,
East Lansing, MI 48824
e-mail: farsad@msu.edu

Shahrokh Zeinali-Davarani
Department of Mechanical Engineering,
Boston University,
Boston, MA 02215
e-mail: zeinalis@bu.edu

Jongeun Choi
Associate Professor
Department of Mechanical Engineering,
Michigan State University,
East Lansing, MI 48824;
Department of Electrical and
Computer Engineering,
Michigan State University,
East Lansing, MI 48824
e-mail: jchoi@egr.msu.edu

Seungik Baek[1]
Associate Professor
Department of Mechanical Engineering,
Michigan State University,
East Lansing, MI 48824
e-mail: sbaek@egr.msu.edu

Computational Growth and Remodeling of Abdominal Aortic Aneurysms Constrained by the Spine

Abdominal aortic aneurysms (AAAs) evolve over time, and the vertebral column, which acts as an external barrier, affects their biomechanical properties. Mechanical interaction between AAAs and the spine is believed to alter the geometry, wall stress distribution, and blood flow, although the degree of this interaction may depend on AAAs specific configurations. In this study, we use a growth and remodeling (G&R) model, which is able to trace alterations of the geometry, thus allowing us to computationally investigate the effect of the spine for progression of the AAA. Medical image-based geometry of an aorta is constructed along with the spine surface, which is incorporated into the computational model as a cloud of points. The G&R simulation is initiated by local elastin degradation with different spatial distributions. The AAA–spine interaction is accounted for using a penalty method when the AAA surface meets the spine surface. The simulation results show that, while the radial growth of the AAA wall is prevented on the posterior side due to the spine acting as a constraint, the AAA expands faster on the anterior side, leading to higher curvature and asymmetry in the AAA configuration compared to the simulation excluding the spine. Accordingly, the AAA wall stress increases on the lateral, posterolateral, and the shoulder regions of the anterior side due to the AAA–spine contact. In addition, more collagen is deposited on the regions with a maximum diameter. We show that an image-based computational G&R model not only enhances the prediction of the geometry, wall stress, and strength distributions of AAAs but also provides a framework to account for the interactions between an enlarging AAA and the spine for a better rupture potential assessment and management of AAA patients.
[DOI: 10.1115/1.4031019]

1 Introduction

Although pathological and biomechanical understanding of AAA and medical imaging techniques has progressed significantly, there is still a pressing need for a reliable prediction of AAA rupture, helping aid patient-specific clinical management. For decades, physicians have conducted a great deal of biomedical engineering research striving to understand why some small AAAs rupture, yet some large AAAs do not [1,2]. Growing evidence provides provisions that have a powerful systematic integration of data-driven specific markers [3,4] and biomechanics [5–7] for a more reliable criterion to determine the rupture risk.

Previous studies promise that quantitative values based on the AAA wall stress and strength are more reliable to determine the rupture risk. The finite element method (FEM) based approaches to calculate the AAA peak wall stress (PWS) [8–10], rupture potential index (RPI) [11], or peak wall rupture risk [3,6] are among such quantitative methods to determine rupture risk. Particularly, active research using FEM has been significantly advanced by incorporating fibrous material properties, patient-specific characteristics, and better damage models with the advantage of evaluating the AAA rupture risk [12–16]. For instance, Forsell et al. [12] employed a data-driven numerical method to estimate the AAA wall's elastic and inelastic properties for each patient-specific case. Their results showed that the mechanical properties were related to the wall thickness, chronic obstructive pulmonary disease, and smoking. Another important study has significantly improved the stress analysis by implementing the residual strain under the physiological pressure [15,17]. Similarly, Reeps et al. presented a 3D FEM model emphasizing the inclusion of thrombus, wall calcification, and prestressed initial state for the AAA with nonlinear hyperelastic material [13]. In addition, Doyle et al. [16] have recently estimated the location of rupture in an AAA wall and verified their results through medical images. Furthermore, using a FEM based fluid–structure interaction (FSI) model, Scotti et al. [18] showed that the AAA wall stress could significantly increase by considering the dynamic effects of the blood pressure. Therefore, these patient-specific biomarkers and biomechanical characteristics promise a better prediction capability for evaluating the risk of the AAA rupture in the near future.

Nevertheless, it is surprising to see that the effect of the surrounding tissue has rarely been taken into account for stress analysis. In most studies of AAA biomechanics, it is assumed that the influence of the surrounding tissue on the AAA is negligible. There is growing evidence suggesting that accounting for the surrounding tissue could be critical for predicting the AAA rupture risk. In a numerical effort, Gasbarro et al. [19] made an explicit finite element model of the current configuration of a descending aorta (with an AAA) along with the spine in order for a FSI AAA analysis. They considered the effects of the dynamics of the blood pressure, the surrounding environment, and the retroperitoneum membrane on the AAA wall mechanics.

Computational G&R models provide time-dependent evolution of biomechanical characteristics of the AAA [20–23], and hence, allow for incorporation of contact due to the aneurysm growth. In our recent studies, we developed a framework for the simulation of AAA expansion initiated by elastin degradation and continuous stress-mediated collagen turnover using realistic geometries [7,24].

Therefore, in this study, we develop a G&R model that is able to implement the contact between the AAA and the spine and

[1]Corresponding author.
Manuscript received November 17, 2014; final manuscript received June 27, 2015; published online July 22, 2015. Assoc. Editor: Jonathan Vande Geest.

 Copyright © 2015 by ASME

Downloaded From: http://biomechanical.asmedigitalcollection.asme.org/ on 07/30/2015 Terms of Use: http://www.asme.org/about-asme/terms-of-use

compute the stress during the AAA expansion. Both geometries of the spine and aorta are captured based on anatomic geometries using computed tomography (CT) scans to enhance the prediction of what happens to the AAA in the future during its expansion. Consequently, we quantify the possible role of interaction between the AAA and the spinal column on changing the AAA biomechanical properties, wall stress distribution, deformation, and collagen fiber content.

2 Method

A computational G&R model is briefly introduced to account for the contact forces between the spine and the AAA during the AAA expansion. The model is also introduced to consider the role of these mechanical stimuli in the biomechanics of the AAA expansion.

2.1 A G&R Model. So far, several computational G&R models have been developed to investigate the effect of time-dependent biomechanical characteristics of an aneurysm (such as stress-mediated collagen fibers generation, degradation, and orientation) on its expansion, stress distribution, and strength [20,21,25–28]. Here, we use a previously developed membrane G&R model, with the details presented in Ref. [7], wherein the main configurations and the mappings between them are depicted in Fig. 1. Three main configurations are defined in this model (Fig. 1): Γ_t denotes the current configuration of an aorta, the pre-stretched configuration Γ_R is defined for computational purposes as the reference configuration, and Γ_τ represents aorta's configuration at time $\tau \in [0, t]$. The aorta's wall is assumed to consist of three main structural constituents: namely, elastin (e) as an isotropic solid, four collagen fiber families ($c^k, k = 1, \cdots, 4$), and smooth muscle (m) oriented circumferentially. Using a constrained mixture approach, collagen fibers and smooth muscle cells turn over continuously over time. The strain energy per unit reference area of constituent i at time t is modeled by

$$w_R^i(t) = M_R^i(0)Q^i(t)\Psi^i(0) + \int_0^t m_R^i(\tau)q^i(\tau,t)\Psi^i(\tau)d\tau \qquad (1)$$

where $M_R^i(0)$ is the mass density of constituent i defined per unit reference area at time 0, $Q^i(t)$ is the mass fraction of constituent i presented at time zero and still exists at time t, $\Psi^i(\tau)$ denotes the strain energy per unit mass of constituent i, $m_R^i(\tau)$ is the stress-dependent rate of mass production of constituent i per unit reference area, and survival function $q^i(\tau,t)$ is the mass fraction of constituent i generated at time τ and still survives at time t. The stress-mediated rate of mass production of the constituent i per unit reference area is given by

$$m_R^i(\tau) = m_b^i \frac{M_R^i(\tau)}{M_R^i(0)}\left[K^i\left(\frac{\sigma^i(\tau)}{\sigma_h^i} - 1\right) + 1\right] \qquad (2)$$

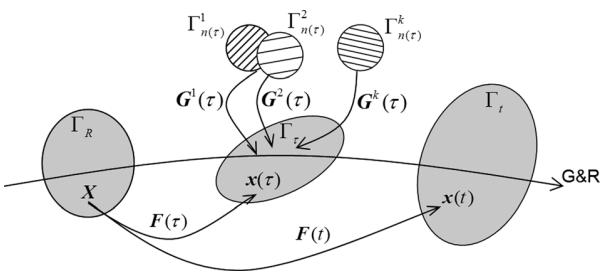

Fig. 1 Different domains from reference (Γ_R) to current (Γ_t) and the corresponding natural configurations for a time $\tau \in [0, t]$. $\mathbf{x}(t)$ denotes the current position vector on the aortic wall, while in reference configuration the position vector is shown by $\mathbf{X}$

where K^i and m_b^i denote scalar values that control the sensitivity of mass production to the membrane stress and the basal rate of mass production, respectively. In addition, $\sigma^i(\tau)$ is a scalar function of Cauchy stress contributed by constituent i at time τ; and σ_h^i is the homeostatic stress for constituent i. The homeostatic stress

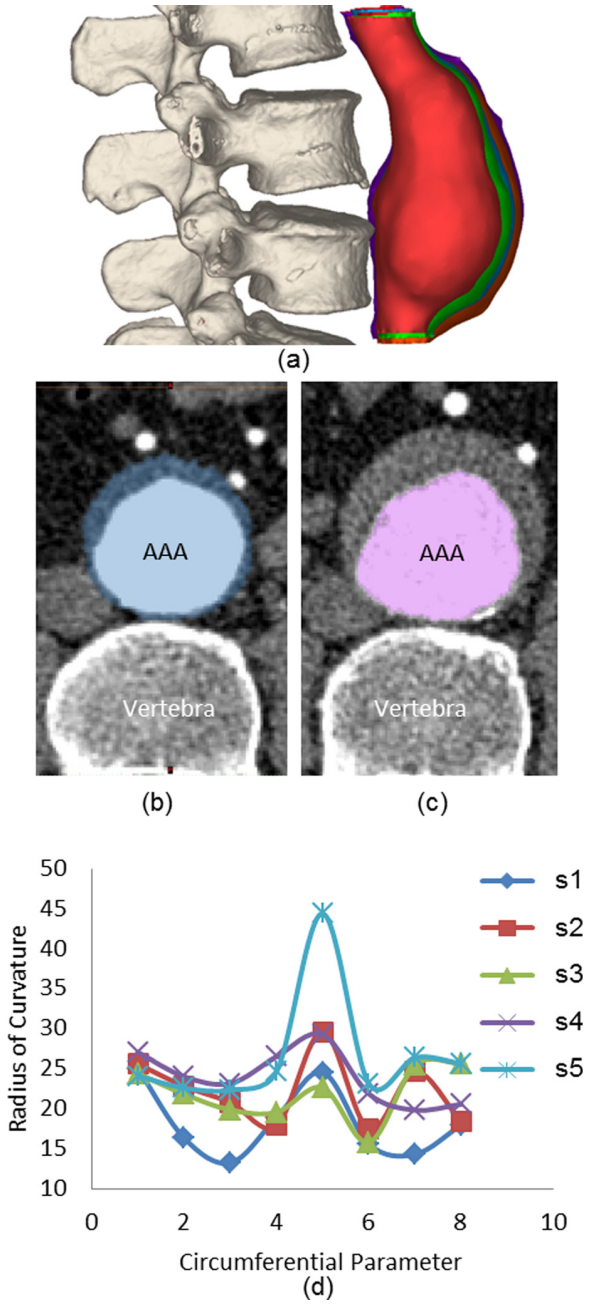

Fig. 2 Significant interaction of a patient's AAA with the spine: (*a*) expansion of the patient's AAA during five longitudinal CT scans (taken during 43 months). The 3D images are built using segmentation software. (*b*) and (*c*) The CT images of the cross section indicating the AAA and the spine contact in the first (s1) and last (s5) scans, respectively. (*d*) The changes of AAA's circumferential radius of curvature in the contact section during the five longitudinal scans (from s1 to s5). The significant increase of circumferential radius of curvature, especially in the last scan, shows flattening of the AAA and its significant interaction with the spine. Circumferential parameter refers to a non-dimensionalized parameter showing the position of a point on the AAA cross section's perimeter, such that the values of 1 and 9 represent $\theta = 0$ and 360 deg, respectively.

Downloaded From: http://biomechanical.asmedigitalcollection.asme.org/ on 07/30/2015 Terms of Use: http://www.asme.org/about-asme/terms-of-use

is obtained according to the stretch that each constituent experiences in healthy in vivo condition in order to maintain the artery's shape [29]. During the progression of the AAA G&R, the blood pressure P is assumed to be constant as the mean pressure during a cardiac cycle. A previous study of longitudinal images of eight patients' AAAs (registered with the vertebral column) speculated that the renal vein and artery, superior mesenteric artery, and iliac bifurcation can serve as anchors (both longitudinal and circumferential) at the superior and inferior boundaries and to the infrarenal AAA during expansion [30]. Hence, it may be possible that the physical constraint of tethering of those vessels provides a strong confinement as anchors. Accordingly, the superior and inferior AAA cross sections are assumed to be fixed at both boundaries.

In the computational G&R framework, it is assumed that the lesion starts at time $t=0$ by loss in elastin mass in a predefined region. At each material point $\mathbf{X}$, the damage ratio at time t is defined by the mass ratio of degenerated elastin to its reference value according to a specific profile. The initial thickness of each constituent, along with the collagen fibers orientation in the artery's wall, is determined through an optimization process satisfying the homeostatic assumption before the damage is introduced [31]. Additionally, it is assumed that elastin cannot be generated after being damaged in an elderly patient, while collagen fibers and smooth muscle cells may be generated or degraded during the G&R as the result of mechanical stimuli in the artery's wall. Although the multiple pathological mechanisms (e.g., inflammation) can be complex for biochemomechanics, it appears that loss of elastic fibers initiates dilation, and the generation or removal of the collagen fibers in the AAA wall is a continuous process to make up the lost mass of the elastin content in order to maintain the artery's stability [32].

Elastin is assumed to behave as an incompressible isotropic neo-Hookean material, while the passive strain energy of all other constituents is given as anisotropic functions. In addition to the passive strain energy, smooth muscle cells incorporate to active tone in vivo such that the level of contraction can change according to its physiological condition. Finally, the total strain energy per unit reference area is given as the summation of passive and active terms. For more details of the specific constitutive strain energy function and stress-mediated constituent turnover, the reader is referred to Ref. [7]. The effect of constitutive formulation on the AAA wall stress can also be found in Ref. [33].

2.2 Accounting for the Effect of AAA–Spine Interaction in the G&R Simulation. In a preliminary study, we investigated a series of longitudinal CT scans of AAA patients. Five scan images of one patient taken over 43 months of surveillance were overlapped (Fig. 2(*a*)). As the AAA expands, the anterior wall bulges while the posterior wall flattens in the contact area against the vertebral column serving as a structural barrier. For instance, see Figs. 2(*b*) and 2(*c*) for the cross-sectional images at the first and the fifth scans of the patient's AAA taken in a period of 43 months. Figure 2(*d*) shows the radius of circumferential curvature for all five scans. This change in geometry may strongly affect the AAA stress and strain distribution. The radius of circumferential curvature, in Fig. 2(*d*), is computed as half of the maximum diameter of each AAA's cross section on the horizontal plane. In addition, for Fig. 2, an iterative global registration algorithm at 1000 iterations with 80% subsample percentage was employed, which minimizes the total distance field between two stereolithography (STL) models of vertebral column. Hence, the vertebral column was considered to be relatively unchanging and of constant shape and size over time. Therefore, it was used as the reference and the shape of AAA's images were overlapped. Those overlapped images shown, however, are only the spatial shapes. The exact locations of the points cannot be identified. Rather than identifying the exact point, the linear growth rate of maximum diameter is used and calculated based on the shape. Martufi et al. [34] addressed the issue and explored different methods of measuring

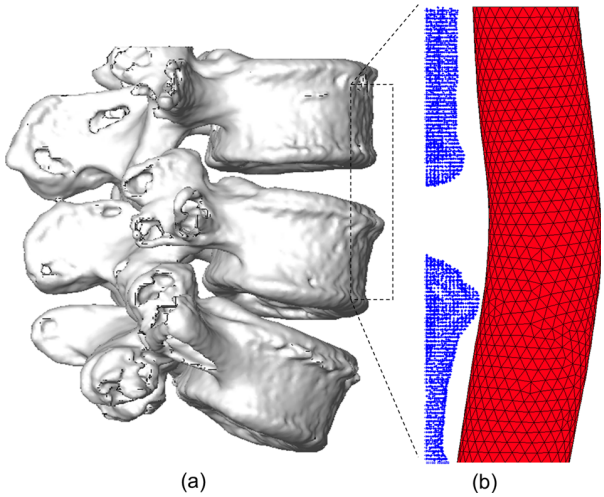

Fig. 3 (*a*) The anatomical model of the vertebral column is constructed from the patient's CT image. (*b*) The computational model of a healthy aorta and probable contact area of the spine as a cloud of points.

growth rate. However, in this paper, we do not take into account those different methods.

To obtain the spine configuration (see Fig. 3(*a*)), the vertebral column was segmented from CT scan images using Mimics (Materialise, Leuven, Belgium). From the segmentation, a 3D

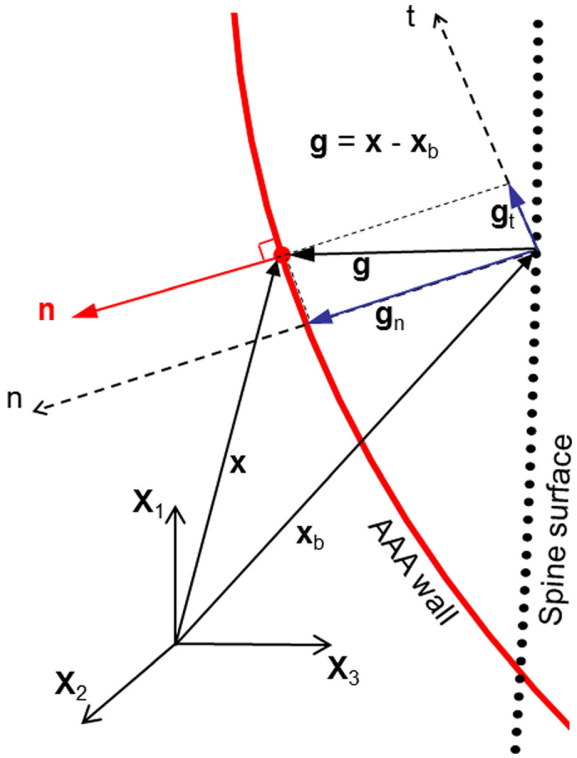

Fig. 4 The schematic view of the AAA penetration into the spine to use in the penalty method. X_1, X_2, and X_3 denote the global principal directions; x and x_b represent the position of a node on the AAA penetrated into the spine and the closest point on the spine surface to x, respectively; n is the outnormal unit vector to the AAA surface; $g = x - x_b$ is the penetration vector and g_n and g_t are the components of the penetration vector along the normal and tangential directions to the AAA surface, respectively.

Downloaded From: http://biomechanical.asmedigitalcollection.asme.org/ on 07/30/2015 Terms of Use: http://www.asme.org/about-asme/terms-of-use

STL model was created and a subjective degree of Laplacian smoothing was performed. For computational purposes, and to avoid unnecessary operations, only a probable contact area on the spine's surface is approximated by a cloud of points as shown in Fig. 3(*b*). Since the spine is relatively rigid, it is assumed to experience no deformation during the G&R process. The initial (healthy) configuration of an aorta, discretized by three-node plane stress elements, is also overlaid in Fig. 3(*b*). Note that the initial aorta's geometry is extracted from a healthy person's CT scans while the spine's geometry is obtained from a patient's CT images, in which the surface of the spine contains calcified regions on the vertebrae edges, which can lead to stress concentration on the AAA wall in the case of contact. Although the space between the spine and the AAA may be filled by adipose tissues, we neglect the stiffness of the adipose tissues in this study based on the AAA–spine contact observed in our preliminary study (see Fig. 2, for example).

The arterial wall, as a membrane with domain Γ_t, interacts with the vertebral column as an external barrier with domain Γ_b in the current configuration. As depicted in Fig. 4, assume that $\mathbf{x}_b$ is the closest point on Γ_b to a node $\mathbf{x}$ on the artery's wall such that the distance $d = |\mathbf{g}|$ is minimized, where $\mathbf{g} = \mathbf{x} - \mathbf{x}_b$. In this paper, the AAA–spine contact is studied under *frictionless* condition. That means only normal penetration g_n is avoided, but tangential relative displacement g_t is allowed with no frictional resistance between the two surfaces. Although there might be some friction at the contact surfaces, it may be reasonable to assume that the frictionless condition is close to the reality to be used in the computational model due to the slippery condition of both surfaces, along with the aneurysm's continuous pulsatile motion and the long time associated with the AAA's evolution. Using a penalty method, a strong spring with stiffness k_p appears only when the node $\mathbf{x}$ on AAA surface penetrates the spine. Otherwise, k_p sets to zero (i.e., there is no contact) [35]. As a result, two points, $\mathbf{x}$ and $\mathbf{x}_b$, approach the contact surface and the penalty term is augmented by the stored energy and given by [35]

$$U_b = \int_{\Gamma_p} \frac{1}{2} k_b g_n^2 d\Gamma_p \tag{3}$$

where Γ_p shows the penetration surface on the artery's wall in the current configuration at time t. In this study, the spine's deformation, and thus its stored energy, vanishes due to its much higher relative stiffness compared to the artery's wall. Therefore, Γ_p should approach Γ_t in the contact region (i.e., $\Gamma_p \subset \Gamma_t$ in Fig. 1). In the other words, any node on the current AAA surface (Γ_t) in which $\mathbf{g} \cdot \mathbf{n} > 0$ is considered to be a member of Γ_p, where the operator "$\cdot$" denotes dot product (see Fig. 4). The contact area (Γ_p) along with each node's penetration ($\mathbf{g}$) are updated at each time step during the numerical solution due to the G&R relevant changes in the AAA geometry. Accordingly, the final weak form for the aortic wall using the principle of virtual work is written as

$$\delta U = \int_{\Gamma_R} \delta W_R d\Gamma_R - \int_{\Gamma_t} P\mathbf{n} \cdot \delta\mathbf{x}\, d\Gamma_t + \int_{\Gamma_p} k_b \delta g_n g_n d\Gamma_p = 0 \tag{4}$$

where W_R denotes the total strain energy of the aortic wall, which is the summation of all constituents' strain energy per unit reference area. P is the mean transmural pressure acting toward the out-normal vector $\mathbf{n}$ to the aorta's wall. The spine undergoes no deformation; thus $\delta\mathbf{x}_b = 0$ that leads to $\delta\mathbf{g} = \delta\mathbf{x}$. As a result, Eq. (4) is rewritten as

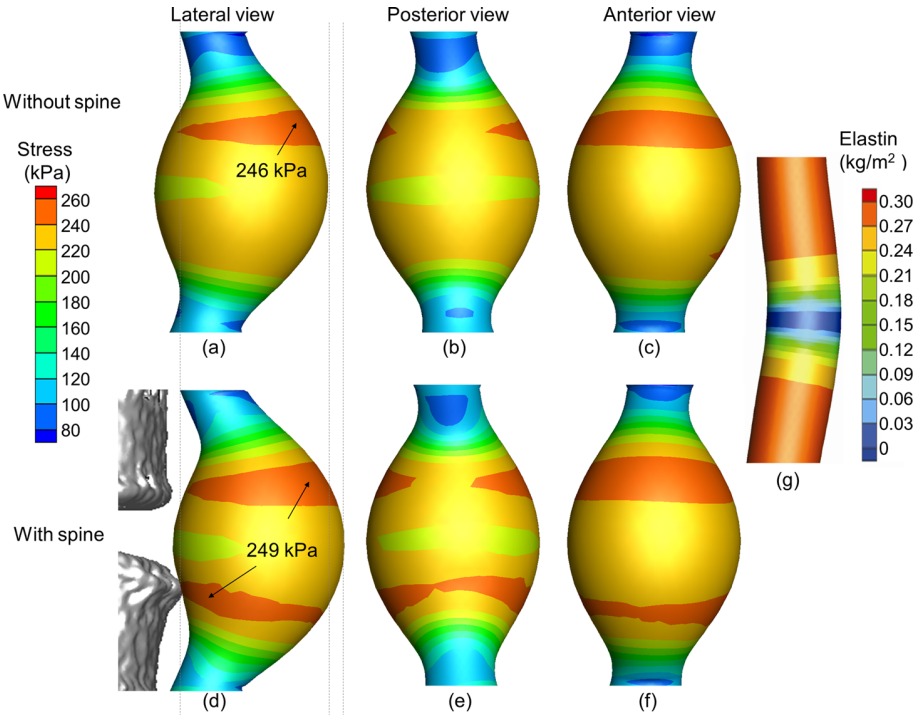

Fig. 5 The von Mises stress distributions of the AAA wall after 3400 days for case 1 (*a*)–(*c*) without the AAA–spine interaction; (*d*)–(*f*) with the AAA–spine interaction in the lateral, posterior, and anterior sides, respectively. (*g*) The elastin distribution for the damage case 1. The arrows and the stress values next to them show the location and the amount of the maximum values, respectively.

Downloaded From: http://biomechanical.asmedigitalcollection.asme.org/ on 07/30/2015 Terms of Use: http://www.asme.org/about-asme/terms-of-use

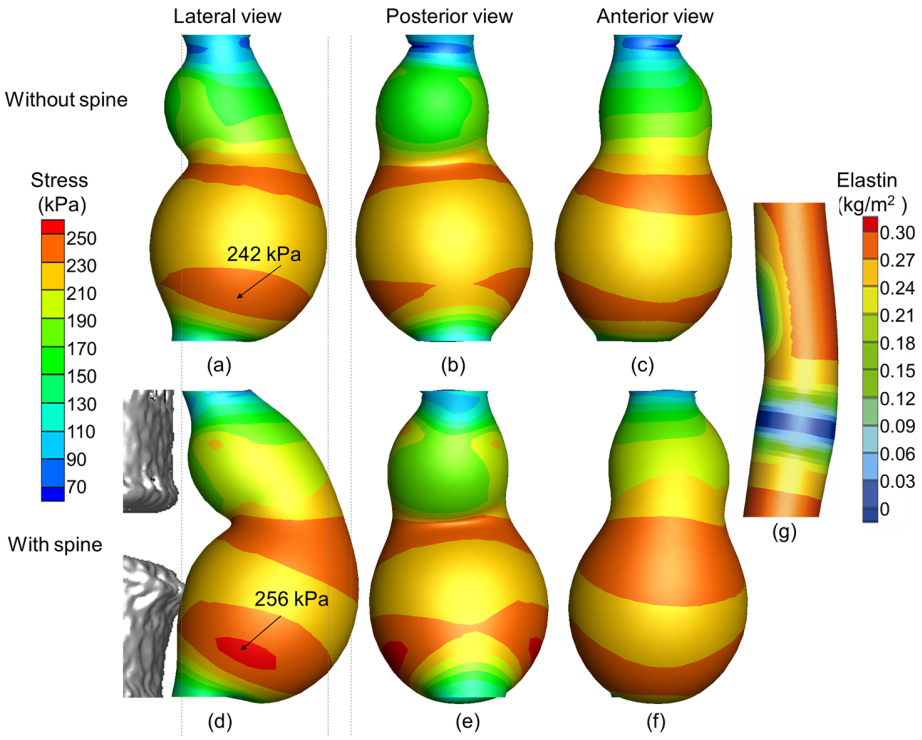

Fig. 6 The von Mises stress distributions of the AAA wall after 3400 days for case 2 (*a*)–(*c*) without the AAA–spine interaction; (*d*)–(*f*) with the AAA–spine interaction in the lateral, posterior, and anterior sides, respectively. (*g*) The elastin distribution for the damage case 2. The arrows and the stress values next to them show the location and the amount of the maximum values, respectively.

$$\delta U = \int_{\Gamma_R} \delta W_R d\Gamma_R - \int_{\Gamma_t} P\mathbf{n} \cdot \delta\mathbf{x}\, d\Gamma_t + \int_{\Gamma_p} k_b(\delta\mathbf{x} \cdot \mathbf{n}) g_n d\Gamma_p = \int_{\Gamma_R} \delta W_R d\Gamma_R - \int_{\Gamma_t} (P - k_b g_n)\mathbf{n} \cdot \delta\mathbf{x}\, d\Gamma_t = 0 \quad (5)$$

where $k_b = 0$ wherever there is no contact between the AAA and spine surfaces (i.e., $\mathbf{g} \cdot \mathbf{n} < 0$). The artery's wall is discretized by triangular plane elements with linear shape functions ϕ_i ($i = 1, 2, 3$). Accordingly, the approximation $\mathbf{x}^h$ for current coordinate $\mathbf{x}$ of a point located in a local element with superscript "e" is written as $\mathbf{x}^h = \Phi\mathbf{x}^e$, where Φ is the usual matrix of shape functions for nodal finite elements. The discretization made above to the presented weak form leads to the following matrix form equation (in order to use in Newton–Raphson solution method):

$$\mathbf{K}^e \Delta\mathbf{x}^e = \mathbf{F}^e \quad (6)$$

where $\mathbf{F}^e$ and $\mathbf{K}^e$ are the residual vector and tangential matrix, respectively. $\mathbf{F}^e$ and $\mathbf{K}^e$ rise from the discretization of the weak form presented in Eq. (4) for the local element with the reference domain Γ_R^e such that

$$F_i^e = F_i^0 e + \int_{\Gamma_p^e} k_p \Phi_{mi}\, n_m\, g_n d\Gamma_p^e \quad (7)$$

$$K_{ij}^e = \frac{\partial F_i^e}{\partial x_j^e} \quad (8)$$

In Eqs. (7) and (8), $i, j = 1, \cdots, 9$ denote an index corresponding to the element's degrees of freedom and $F_i^0 e$ results from discretization of the first two terms of Eq. (4). The last term in Eq. (7) appears only if node $\mathbf{x}$ penetrates the spine. In this case, in according to Fig. 4, $\mathbf{g}$ is calculated for each Gauss point on the AAA surface by connecting it to the closest point on the spine point cloud. In addition, g_n is the projection of $\mathbf{g}$ on the normal direction to the AAA surface at the element Gauss point. Furthermore, $\Gamma_p^e \subset \Gamma_t^e$ represents a subset of the domain of a local element (i.e., a subset of the element's Gauss points) in the current configuration in which the artery's wall has penetrated the spine. The details of all other terms including finite element discretization and governing equations may be found in Ref. [24].

3 Results

As discussed in Sec. 2, the AAA is initiated by the instantaneous loss of elastin in a predefined region. In this section, we study two distinct profiles for elastin degradation distribution. Case 1 depicted in Fig. 5(*g*) shows a circumferentially uniform degradation distribution in the middle of the simulated part from an unaneurysmatic aorta. Case 2 represents circumferentially uniform damage in the lower half of the simulated part of the aorta and a concentrated damaged region on the posterior side of the upper half (Fig. 6(*g*)). Case 1 is chosen because it represents a typical aneurysm with one sac only, while case 2 results in a more complicated AAA geometry with two sacs. A more severe AAA–spine interaction is expected in case 2, since the regions with elastin degradation are located exactly in front of two vertebrae. We are also interested in the second sac after the first one contacts the spine in case 2. All other model parameters are the same in cases 1 and 2 and are shown in Table 1. Both cases are investigated in our computational simulations with and without the AAA–spine interaction up to 3400 days of G&R.

Figures 5 and 6 illustrate the final configurations as well as the resultant von Mises stress distributions in the AAA wall for cases 1 and 2, respectively. Each figure depicts the results for the situation in which the AAA expands freely without facing an external

Downloaded From: http://biomechanical.asmedigitalcollection.asme.org/ on 07/30/2015 Terms of Use: http://www.asme.org/about-asme/terms-of-use

Table 1 The model variables used in Eq. (2) in order for the numerical simulations. All the values are taken from Ref. [24].

K^c	K^c	P (Pa)	m_b^c(kg/sm^2)	m_b^m(kg/sm^2)	σ_h^c(Pa)	σ_h^m(Pa)	$M_R^e(0)$(kg/m^2)	$M_R^c(0)$(kg/m^2)	$M_R^m(0)$(kg/m^2)
0.05	0.05	13,600	8.299×10^{-04} 8.299×10^{-04} 1.245×10^{-03} 1.245×10^{-03}	4.15×10^{-03}	135,000	81,000	0.272	0.204	0.204

barrier as well as the condition when the vertebral column limits the AAA expansion as a constraint. Both cases in Figs. 5(*d*) and 6(*d*) illustrate significant changes in final geometries of the simulated AAAs when interacting with the spine. When the simulated AAAs interact with the spine, they show more expansion in the anterior side than those without AAA–spine interaction. The contact leads to an increased curvature in the AAA wall, especially in case 2. This results in no contact between the spine and the upper AAA sac in case 2 (see Figs. 6(*a*) and 6(*d*)).

The von Mises stress (Figs. 5 and 6) increases in the vicinity of the contact region. Furthermore, von Mises stress is elevated in the lateral and anterior sides of the simulated AAA walls under the contact condition with the spine.

Figure 7 shows the asymmetry of the simulated AAAs after 3400 days with respect to the normalized longitudinal distance and the changes of their maximum asymmetry during time. The same concept, as defined by Doyle et al. [36], was adopted for the definition of asymmetry which is determined by the perpendicular distance of a point on the centerline to the straight line connecting the distal and proximal points. Figure 7 shows that AAA's asymmetry significantly increases as a result of interacting with the spine.

In addition, Figs. 8 and 9 depict the distribution of AAA wall stretch along longitudinal and circumferential directions for case 1 and case 2, respectively. It is shown in the figure that while there is no significant change in maximum circumferential stretch, maximum stretch increases slightly as the result of AAA–spine interaction, particularly in case 2.

Figures 10 and 11 illustrate the collagen fiber concentration (per current area) in the AAA wall for cases 1 and 2 with and without the AAA–spine contact. The regions of higher collagen content coincide with the regions of higher degradation of elastin (Figs. 5(*d*) and 6(*d*)). The collagen content is similar between the conditions of with and without the AAA–spine interaction in case 1 (Fig. 10). But the collagen content in case 2 significantly increases in the posterior side of the neck between the bulges and decreases in the vicinity of contact region when the AAA interacts with the spine (Fig. 11).

4 Discussion

In the last decade, significant progress has been made toward patient-specific computational rupture risk assessment of AAAs. The majority of the studies focused on stress analysis of the AAA wall in a specific time point during the progression of the disease [3,6,8,10,37–40], suggesting that wall stress is a better estimator of rupture potential than the "maximum diameter criterion" on a patient-to-patient basis. Furthermore, a separate category of studies focused on the dynamic adaptive processes by which AAA wall grows and remodels [7,20,25]. The latter studies not only track the evolving morphological properties of AAAs but also provide a window of opportunity to evaluate changes in the wall material and structural properties and, thus, wall strength (see review by Humphrey and Holzapfel [32]). Proper assumptions regarding the boundary conditions including perivascular tissues

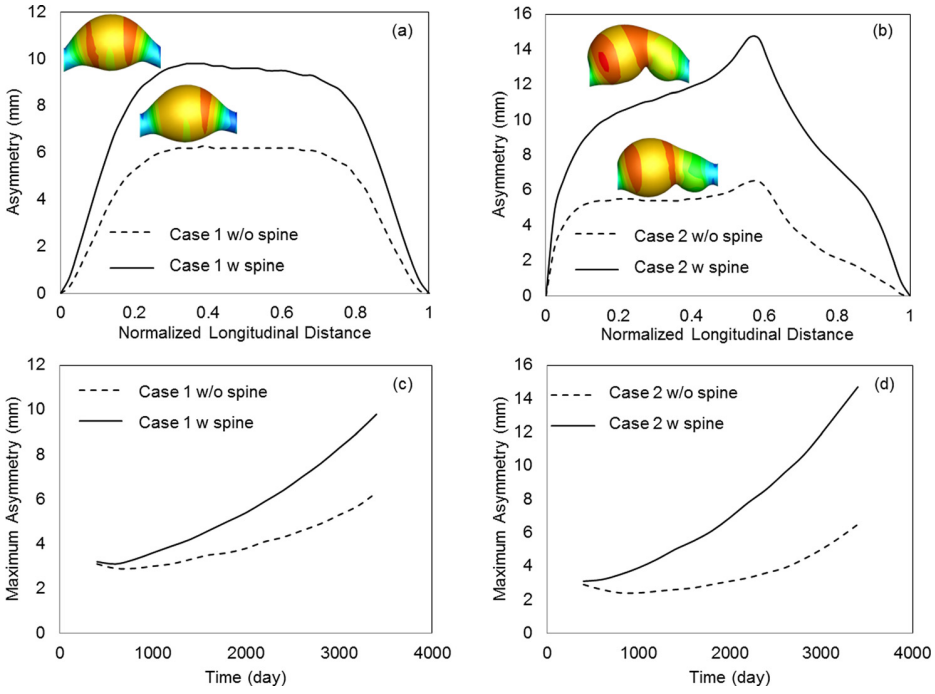

Fig. 7 (*a*) and (*b*) The changes of simulated AAAs' final asymmetry along the AAA after 3400 days. (*c*) and (*d*) The changes of simulated AAAs maximum asymmetry during time. Asymmetry is calculated using the definition represented by Doyle et al. [36] based on the perpendicular distance of any point on the AAA's centerline from the straight line connecting end points of the centerline.

Downloaded From: http://biomechanical.asmedigitalcollection.asme.org/ on 07/30/2015 Terms of Use: http://www.asme.org/about-asme/terms-of-use

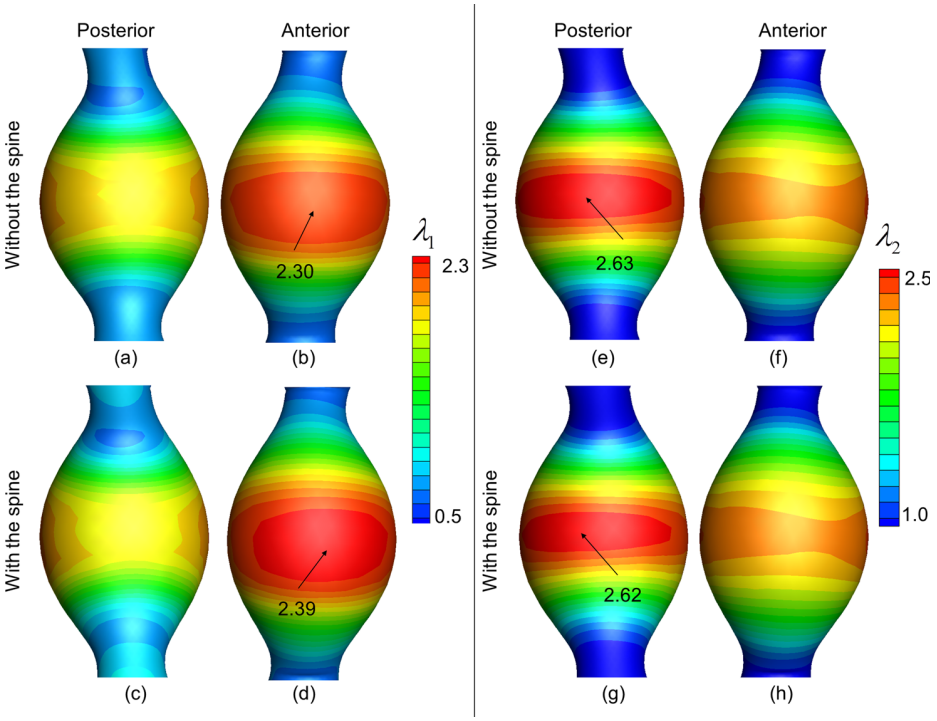

Fig. 8 The final distribution of simulated AAAs wall stretch for case 1 along longitudinal (*a*)–(*d*) and circumferential (*e*)–(*g*) directions with and without AAA–spine interaction. λ_1 and λ_2 are longitudinal and circumferential stretches, respectively, from reference to current configuration. The values shown next to the arrows denote the maximum values.

could have a defining role in the biomechanical and mechanobiological assessments of AAAs in both types of studies.

Aortic aneurysms are likely to be physically constrained by the spine (for example, see Fig. 2). Ruiz et al. [41] and Sugiu et al. [42] investigated the influence of a perianeurysmal environment on ruptured and unruptured cerebral aneurysms and showed that the contact with the perianeurysmal environment influenced the shape and rupture potential of aneurysms. It is intuitively

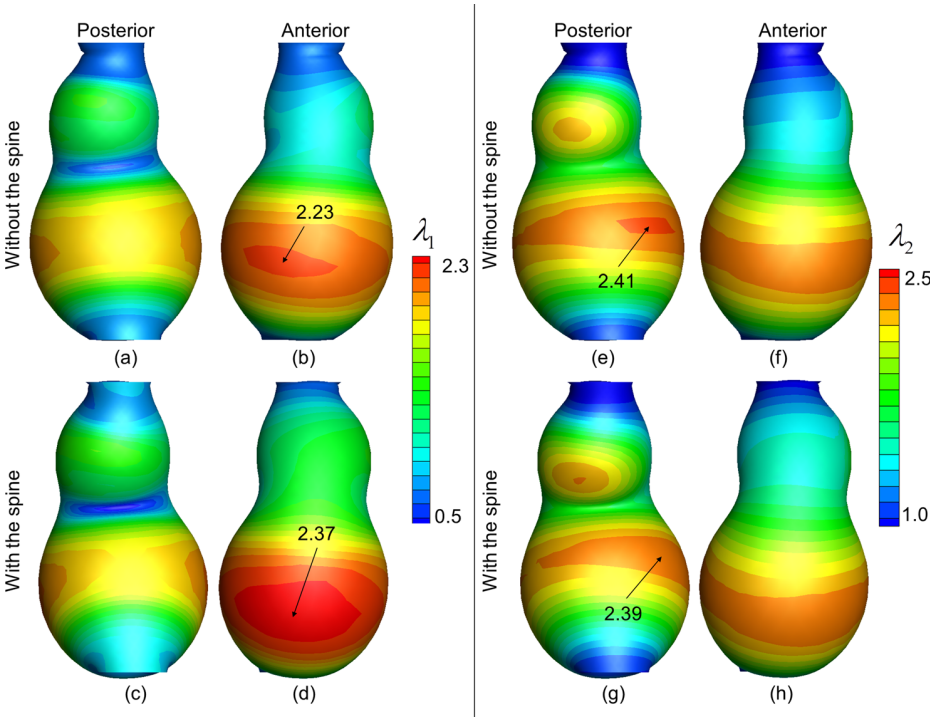

Fig. 9 The final distribution of simulated AAAs wall stretch for case 2 along longitudinal (*a*)–(*d*) and circumferential (*e*)–(*g*) directions with and without AAA–spine interaction. λ_1 and λ_2 are longitudinal and circumferential stretches, respectively, from reference to current configuration. The values shown next to the arrows denote the maximum values.

Downloaded From: http://biomechanical.asmedigitalcollection.asme.org/ on 07/30/2015 Terms of Use: http://www.asme.org/about-asme/terms-of-use

important to analyze whether the spine contact has a protective role, through perivascular tethering [43–46] or a deleterious impact on AAA biomechanics. Nevertheless, the contact forces are not only unknown in vivo but also changing as the AAA and contact surfaces evolve, making it difficult for the standard patient-specific stress analyses of AAAs to account for the contact forces. On the other hand, computational G&R models facilitate studying the time-dependent role of the spine as a contact constraint on aneurysm expansion without the direct knowledge of contact forces.

In this paper, we modified a previously developed framework for simulation of realistic AAA G&R [7,24] to account for the contact between a growing AAA and the spine column with geometrical features of contact using the penalty method. We showed that when the posterior surface of the AAA reaches the spine, the expansion is significantly limited on that contact side while the lesion flattens out, consistent with a longitudinal study of multiple AAA patients (for example, see Fig. 2). However, on the anterior and lateral sides, the aneurysm is free to expand while pushing against the spine. Both simulation conditions, with and without AAA–spine interaction, resulted in the same AAA's rate of expansion (Fig. 12), suggesting that AAA–spine interaction may not necessarily affect the expansion rate. This is consistent with the fact that maximum stress with spine interaction seems to be only slightly increased from the case with no interaction. Figure 12(*b*) shows the computed range of maximum diameter's rate compared with that of the clinical data analysis performed in Ref. [47]. Watton et al. [25] were the first to study the effects of the spine (as a rigid plane) in an idealized model of evolving aneurysms. They found a preferential bulging on the anterior side of their AAA model. Considering the periodic nature of the aortic or AAA wall (radial) motion, it is reasonable to assume that there is minimal permanent attachment between AAAs and the spine and that the AAA wall can move tangential to the spine. Therefore, we believe the frictionless contact assumption is more realistic than the tied contact assumption.

The results illustrated that geometrical features such as asymmetry (eccentricity), curvature, and tortuosity are considerably affected in the presence of AAA–spine interaction (see Fig. 7). Those geometrical features are suggested as diagnostic tools in the assessment of AAAs rupture potential [4,36]. Furthermore, Figs. 8 and 9, together with the average values in Table 2, indicate that there is not a significant change in circumferential stretch in the AAA wall when there is AAA–spine interaction compared to when there is no contact. It means the maximum diameter of the AAA does not change significantly as the result of interacting with the spine. On the other hand, it is indicated that the longitudinal stretch increases slightly (from 1.54 to 1.57 and from 1.48 to 1.55 for cases 1 and 2, respectively). This change in the average longitudinal stretch, as the result of interacting with the spine, is in agreement with AAA lengthening and increase in the asymmetry of AAA due to interacting with the spine. Even though spine contact did not significantly change the PWS (from 246 kPa to 249 kPa in case 1 and from 242 kPa to 256 kPa in case 2), the stress is elevated particularly in the shoulder region, as a result of the AAA–spine interaction (Figs. 5 and 6). In addition, Table 2 shows a 36% and 40% increase in the average wall stress compared to the initial condition, while the increase in wall stress is only about 2% and 5% when there is no spine constraining the AAA growth in cases 1 and 2, respectively. The small difference in maximum stress between with and without AAA–spine interaction conditions is consistent with the fact that the growth rate is also not very different. It is likely that framework is more sensitive to G&R parameters as well as the distribution of initial insult

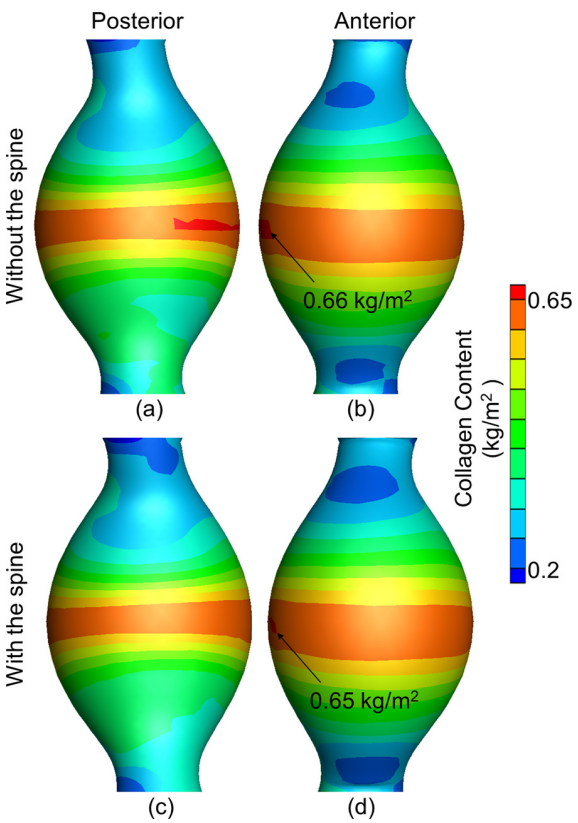

Fig. 10 The collagen fiber content in the AAA wall after 3400 days for case 1. (*a*) and (*b*) The posterior and anterior view without the AAA–spine interaction. (*c*) and (*d*) The posterior and anterior view with the AAA–spine interaction.

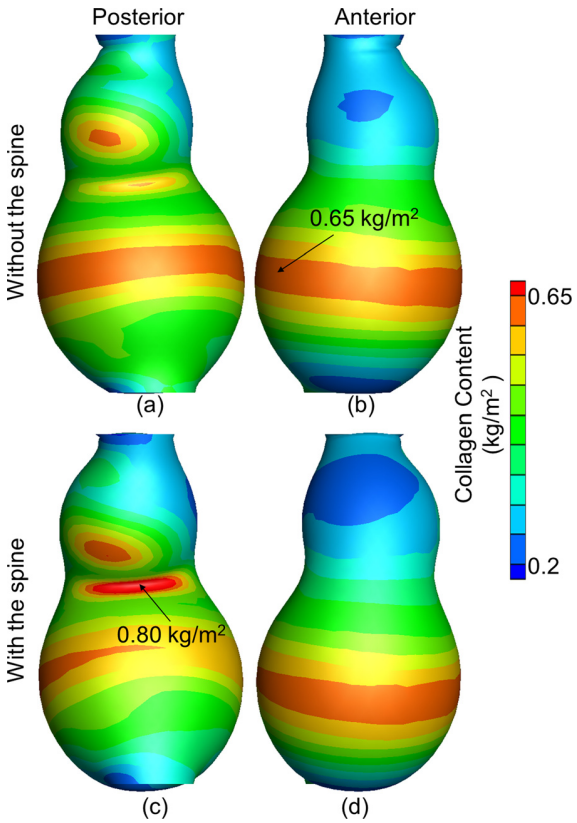

Fig. 11 The collagen fiber content in the AAA wall after 3400 days for case 2. (*a*) and (*b*) The posterior and anterior view without the AAA–spine interaction. (*c*) and (*d*) The posterior and anterior view with the AAA–spine interaction.

Downloaded From: http://biomechanical.asmedigitalcollection.asme.org/ on 07/30/2015 Terms of Use: http://www.asme.org/about-asme/terms-of-use

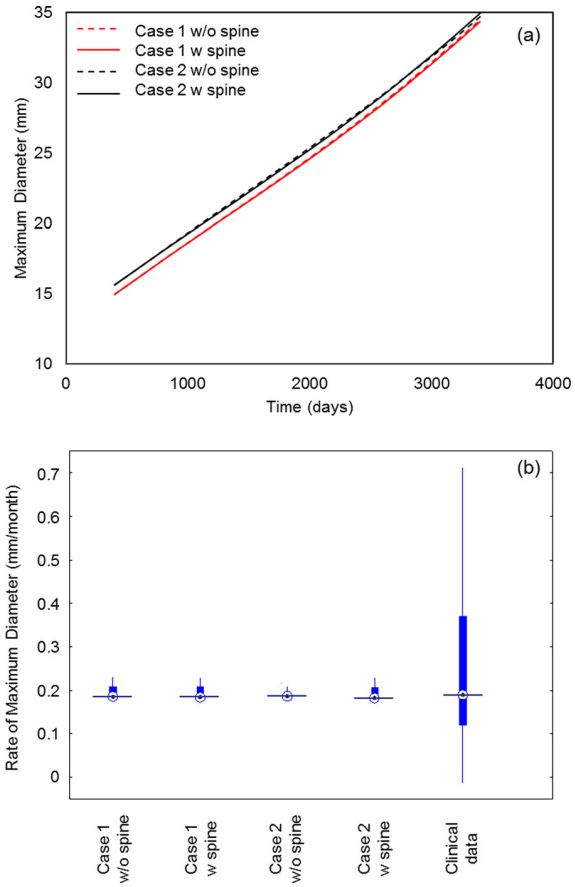

Fig. 12 (*a*) The changes of the simulated AAAs' maximum diameter versus time. (*b*) Comparison between the computational and clinical rate of maximum diameter versus time. The longitudinal CT data from 14 patients are used in Ref. [47].

in elastin than to the AAA wall–spine interaction. A parameter sensitivity study could better reveal the impact of spine interaction on rupture risk analysis. Statistical analysis to compare spatial distribution of variables (e.g., stress and collagen content) is ultimately needed to verify the statistical significance of our results.

In simulation results with no spine interaction, the average collagen fibers content per current area showed about two-fold increase (from 0.2278kg/m^2 to 0.4300kg/m^2 for case 1 and to 0.4405 for case 2) due to the stress-mediated collagen deposition on the damaged regions (Table 2). The lower content of collagen in the contact region (Figs. 11(*a*) and 11(*c*)) may be explained by the altered expansion of the wall on the contact region. The increase in the collagen content in the neck regions (Fig. 11(*c*)) can be the result of the AAA wall being compressed in that region leading to an elevated collagen fiber areal density [24]. However, a simplified collagen structure (four families of fibers) is assumed in this paper that leads to formation or degradation of collagen along certain directions and inducing some limitation in the presented framework. In future, continuous fiber distribution models, such as what was proposed in Refs. [5] and [48], should be employed for better representation of the collagen structure.

Following Zeinali-Davarani et al. [7,31], smooth muscle cell content is degraded simultaneously at the beginning of simulation proportional to the elastin loss. After this point, the sensitivity of smooth muscle content in the presented framework is not as significant as collagen fiber. The average amount of smooth muscle for different cases (Table 2) shows that although the total amount of smooth muscle content (M_m) increases during G&R due to increase in the AAA wall, the distribution of smooth muscle per current area (m_m) is kept almost the same as the initial value (0.1809kg/m^2). This finding is in contrast with what resulted by Lopez-Candales et al. [49] in which it is emphasized that smooth muscle content shows 74% decrease in the late stage aneurysm. The reason for this contrast might be first, the numerical aneurysms are probably still too far from the late stage, and second, wall shear stress is not considered in the smooth muscle tone in this paper, although it can play an important role in formation or dissociation of smooth muscle content.

The effects of the intraluminal thrombus (ILT) thickness, sex, family history, and smoking on the AAA strength have been well examined in computational models of AAAs [3,50]. In addition, Di Martino et al. [51] suggested a weak (but significant) negative correlation ($R=-0.42$ and $P=0.012$) between the AAA wall thickness and its tensile strength. Using their patients' data, we regenerated the trend line estimating the linear relation between the AAA wall thickness (h in mm) and the AAA wall tensile strength (σ_u in kPa) such that $\sigma_u=-170.43h+1224.7$. In order to find the trend line, a linear regression is performed on the data without deleting any data. Thereby, we estimated the local wall strength based on wall thickness and used the ratio of first principal stress to the tensile strength as an indicator of regions with high rupture risk (Fig. 13). The highest ratio appears on the posterior side of the neck between the two bulges (in case 2) as well as the posterolateral sides (in both cases 1 and 2). Although the maximum ratio is only moderately elevated from 0.251 to 0.255 and from 0.251 to 0.278 in cases 1 and 2, respectively, the upper bulge in case 2 shows a significant increase in the stress (Fig. 6) and stress-to-strength ratio (Fig. 13) on the lateral and anterior sides despite having no contact with the spine. It should be emphasized here that the ratios in Fig. 13 are believed to be in good correlation with rupture risk, although they are not the precise estimation for the RPI. For a better estimation of rupture risk, other factors such as ILT and gender should be taken into account.

Veldenz et al. [52] showed that in rapidly expanding small aneurysms the posterolateral side has a larger radius of curvature, implying higher local wall tensions according to the Laplace law. Doyle et al. [36] found that expansion of AAAs on one side induces elevated wall stress on the opposite side. These findings are consistent with higher wall stress and the stress-to-strength ratio in the posterolateral regions of our simulated aneurysms as they expand on the anterior side (Figs. 6(*d*), 13(*b*), and 13(*d*)). The spine plays a protective role for the posterior side of the AAA

Table 2 The average amount (calculated over the whole AAA surface) of von Mises stress VMS, longitudinal stretch λ_1, circumferential stretch λ_2, collagen content per reference area M_c, collagen content per current area m_c, smooth muscle content per reference area M_m, and smooth muscle content per current area m_m. The initial values refer to the situation where all the content and collagen fiber orientation are optimized to conform with the homeostatic condition.

Case	VMS (kPa)	λ_1	λ_2	$M_c(\text{kg/m}^2)$	$M_m(\text{kg/m}^2)$	$m_c(\text{kg/m}^2)$	$m_m(\text{kg/m}^2)$
Initial	153.5690	0.9961	1.0108	0.2278	0.1809	0.2278	0.1809
Case1 w/o the spine	205.0463	1.5430	1.8563	1.5624	0.4048	0.4300	0.1843
Case1 w the spine	208.6753	1.5683	1.8415	1.5496	0.3965	0.4231	0.1794
Case2 w/o the spine	202.5526	1.4796	1.8443	1.4421	0.3651	0.4405	0.1814
Case2 w the spine	213.1120	1.5509	1.8385	1.4353	0.3667	0.4243	0.1709

Downloaded From: http://biomechanical.asmedigitalcollection.asme.org/ on 07/30/2015 Terms of Use: http://www.asme.org/about-asme/terms-of-use

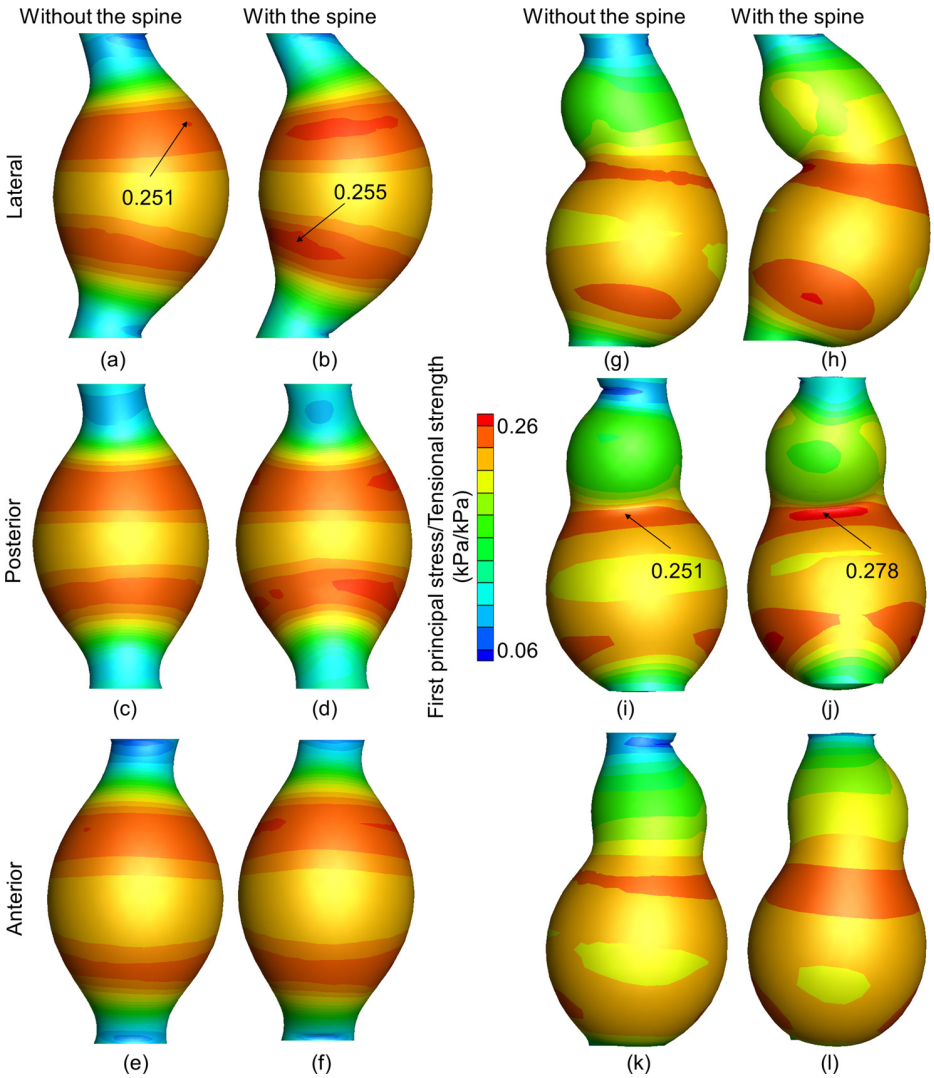

Fig. 13 The ratio of the first principal stress to the tensile strength in the AAA wall after 3400 days for case 1 (*a*)–(*f*) and case 2 (*g*)–(*l*) for the conditions with and without AAA–spine interaction

wall by tethering. As a result the AAA, which commonly does not rupture in the supported region, usually ruptures in the posterolateral sites due to the retroperitoneal cavity [1]. On the other hand, higher surface curvature [53] and centerline asymmetry [54] have been associated with higher wall stress. Patient-specific aneurysm models were shown to rupture mostly at regions of high stress (inflection regions) [36,55] which were not necessarily the regions of lowest wall thickness. Consistently, in hypothetical aneurysm models [56] found that the inflection regions are subject to the highest stress. Thus, the AAA shape, size, and wall thickness distribution altogether contribute to the complex wall stress distribution which is markedly evolving as the AAA enlarges [4]. We submit that morphological features alone may not be sufficient to determine the rupture potential. Therefore, the local G&R as well as contact constraints should also be taken into account.

There are several limitations associated with this study. Although the aneurysmal wall is thin compared to its diameter, our computationally simulated AAAs are initially generated from a nonaneurysmal aortic geometry, in which the bending stiffness may not be negligible. The presence of a heavy thrombus layer or calcified regions also demands advanced models that account for the increased bending stiffness. We speculate that the inclusion of bending stiffness in our analysis intensifies the effects of spine contact on the morphology, wall stress distribution, and PWS, beyond what we observed in this study. Accurate measures of wall strength are yet to be considered in our analysis for a reliable assessment of rupture [50,51,57,58]. Our simulation cases represent hypothetical models of AAAs initiated by artificial elastin degradation in a healthy aorta instead of the real elastin loss in a patient's AAA wall. Recently, we have had access to longitudinal CT images of 14 patients (more than 60 images) that could be used in the ongoing research to estimate a realistic elastin damage shape using estimation techniques. There is recent progress toward estimating the model parameters [59], calibrating the model, and considering the biochemomechanical effects of ILT on the AAA G&R using patients' longitudinal CT images [60]. The outcome of these ongoing studies will help validating the proposed G&R computational model and strengthens its predictive capabilities. Despite these limitations, this initial study has shed light on the possible role of the spine as a physical barrier of AAA G&R for the clinical management of AAA patients.

Acknowledgment

Authors gratefully acknowledge the support, in part, by the NHLBI NIH under R01HL115185 and the NSF under CAREER

Downloaded From: http://biomechanical.asmedigitalcollection.asme.org/ on 07/30/2015 Terms of Use: http://www.asme.org/about-asme/terms-of-use

CMMI-1150376. Authors gratefully acknowledge Sebastian T. Kwon for his assistance on the patients' CT images study.

References

[1] Darling, R. C., Messina, C. R., Brewster, D. C., and Ottinger, L. W., 1977, "Autopsy Study of Unoperated Abdominal Aortic Aneurysms. The Case for Early Resection," Circulation, **56**(Suppl. 3), pp. 161–164.

[2] Nicholls, S. C., Gardner, J. B., and Johansen, M. H. M. K., 1998, "Rupture in Small Abdominal Aortic Aneurysms," J. Vasc. Surg., **28**(5), pp. 884–888.

[3] Maier, A., Gee, M. W., Reeps, C., Pongratz, J., Eckstein, H. H., and Wall, W. A., 2010, "A Comparison of Diameter, Wall Stress, and Rupture Potential Index for Abdominal Aortic Aneurysm Rupture Risk Prediction," Ann. Biomed. Eng., **38**(10), pp. 3124–3134.

[4] Shum, J., Martufi, G., Di Martino, E., Washingtom, C. B., Grisafi, J., Muluk, S. C., and Finol, E. A., 2011, "Quantitative Assessment of Abdominal Aortic Aneurysm Geometry," Ann. Biomed. Eng., **39**(1), pp. 277–286.

[5] Gasser, T. C., Ogden, R. W., and Holzapfel, G. A., 2006, "Hyperelastic Modelling of Arterial Layers With Distributed Collagen Fibre Orientations," J. R. Soc. Interface, **3**(6), pp. 15–35.

[6] Gasser, T. C., Auer, M., Labruto, F., Swedenborg, J., and Roy, J., 2010, "Biomechanical Rupture Risk Assessment of Abdominal Aortic Aneurysms: Model Complexity Versus Predictability of Finite Element Simulations," Eur. J. Vasc. Endovasc. Surg., **40**(2), pp. 176–185.

[7] Zeinali-Davarani, S., Sheidaei, A., and Baek, S., 2011, "A Finite Element Model of Stress-Mediated Vascular Adaptation: Application to Abdominal Aortic Aneurysms," Comput. Methods Biomech. Biomed. Eng., **14**(9), pp. 803–817.

[8] Fillinger, M. F., Raghavan, M. L., Marra, S. P., Cronenwell, J. L., and Kennedy, F. E., 2002, "In Vivo Analysis of Mechanical Wall Stress and Abdominal Aortic Aneurysm Rupture Risk," J. Vasc. Surg., **36**(3), pp. 589–597.

[9] Heng, M. S., Fagan, M. J., Collier, J. W., Desai, G., McCollum, P. T., and Chetter, I. C., 2008, "Peak Wall Stress Measurement in Elective and Acute Abdominal Aortic Aneurysms," J. Vasc. Surg., **47**(1), pp. 17–22.

[10] Venkatasubramaniam, A. K., Fagan, M. J., Mehta, T., Mylankal, K. J., Ray, B., Kuhan, G., Chetter, I. C., and McCollum, P. T., 2004, "A Comparative Study of Aortic Wall Stress Using Finite Element Analysis for Ruptured and Non-Ruptured Abdominal Aortic Aneurysms," Eur. J. Vasc. Surg., **28**(2), pp. 168–176.

[11] Vande Geest, J. P., Di Martino, E. S., Bohra, A., Makaroun, M. S., and Vorp, D. A., 2006, "A Biomechanics-Based Rupture Potential Index for Abdominal Aortic Aneurysm Risk Assessment: Demonstrative Application," Ann. N. Y. Acad. Sci., **1085**, pp. 11–21.

[12] Forsell, C., Swedenborg, J., Roy, J., and Gasser, T. C., 2013, "The Quasi-Static Failure Properties of the Abdominal Aortic Aneurysm Wall Estimated by a Mixed Experimental-Numerical Approach," Ann. Biomed. Eng., **41**(7), pp. 1554–1566.

[13] Reeps, C., Gee, M., Maier, A., Gurdan, M., Eckstein, H.-H., and Wall, W. A., 2010, "The Impact of Model Assumptions on Results of Computational Mechanics in Abdominal Aortic Aneurysm," J. Vasc. Surg., **51**(3), pp. 679–688.

[14] Marini, G., Maier, A., Reeps, C., Eckstein, H.-H., Wall, W. A., and Gee, M. W., 2012, "A Continuum Description of the Damage Process in the Arterial Wall of Abdominal Aortic Aneurysms," Int. J. Numer. Methods Biomed. Eng., **28**(1), pp. 87–99.

[15] Polzer, S., Bursa, J., Gasser, T. C., Staffa, R., and Vlachovski, R., 2013, "A Numerical Implementation to Predict Residual Strains From the Homogeneous Stress Hypothesis With Application to Abdominal Aortic Aneurysms," Ann. Biomed. Eng., **41**(7), pp. 1516–1527.

[16] Doyle, B. J., McGloughlin, T. M., Miller, K., Powell, J. T., and Norman, P. E., 2014, "Regions of High Wall Stress Can Predict the Future Location of Rupture of Abdominal Aortic Aneurysm," Cardiovasc. Interventional Radiol., **37**(3), pp. 815–818.

[17] Raut, S. S., Chandra, S., Shum, J., and Finol, E. A., 2013, "The Role of Geometric and Biomechanical Factors in Abdominal Aortic Aneurysm Rupture Risk Assessment," Ann. Biomed. Eng., **41**(7), pp. 1459–1477.

[18] Scotti, C. M., Jimenez, J., Muluk, S. C., and Finol, E. A., 2008, "Wall Stress and Flow Dynamics in Abdominal Aortic Aneurysms: Finite Element Analysis vs. Fluid-Structure Interaction," Comput. Methods Biomech. Biomed. Eng., **11**(3), pp. 301–322.

[19] Gasbarro, M. D., Shimada, K., and Di Martino, E. S., 2007, "Explicit Finite Element Method for In-Vivo Mechanics of Abdominal Aortic Aneurysm," Eur. J. Comput. Mech., **16**(3–4), pp. 337–363.

[20] Baek, S., Rajagopal, K. R., and Humphrey, J. D., 2006, "A Theoretical Model of Enlarging Intracranial Fusiform Aneurysms," ASME J. Biomech. Eng., **128**(1), pp. 142–149.

[21] Watton, P. N., and Hill, N. A., 2009, "Evolving Mechanical Properties of a Model of Abdominal Aortic Aneurysm," Biomech. Model. Mechanobiol., **8**(1), pp. 25–42.

[22] Martufi, G., and Gasser, T. C., 2012, "Turnover of Fibrillar Collagen in Soft Biological Tissue With Application to the Expansion of Abdominal Aortic Aneurysms," J. R. Soc., **9**(77), pp. 3366–3377.

[23] Valentin, A., and Holzapfel, G. A., 2012, "Constrained Mixture Models as Tools for Testing Competing Hypotheses," Mech. Res. Commun., **42**, pp. 126–133.

[24] Zeinali-Davarani, S., and Baek, S., 2012, "Medical Image-Based Simulation of Abdominal Aortic Aneurysm Growth," Mech. Res. Commun., **42**, pp. 107–117.

[25] Watton, P. N., Hill, N. A., and Heil, M., 2004, "A Mathematical Model for the Growth of the Abdominal Aortic Aneurysm," Biomech. Model. Mechanobiol., **3**(2), pp. 98–113.

[26] Kroon, M., and Holzapfel, G. A., 2007, "A Model for Saccular Cerebral Aneurysm Growth by Collagen Fibre Remodelling," J. Theor. Biol., **247**(4), pp. 775–787.

[27] Kroon, M., and Holzapfel, G. A., 2009, "A Theoretical Model for Fibroblast-Controlled Growth of Saccular Cerebral Aneurysms," J. Theor. Biol., **257**(1), pp. 73–83.

[28] Hariton, I., deBotton, G., Gasser, T. C., and Holzapfel, G. A., 2007, "Stress-Driven Collagen Fiber Remodeling in Arterial Walls," Biomech. Model. Mechanobiol., **6**(3), pp. 163–175.

[29] Humphrey, J. D., and Rajagopal, K. R., 2002, "A Constrained Mixture Model for Growth and Remodeling of Soft Tissues," Math. Models Methods Appl. Sci., **12**(3), pp. 407–430.

[30] Dupay, A. C., 2012, "Investigation of Surface Evolution for Abdominal Aortic Aneurysms Interacting With Surrounding Tissues," MSc. thesis, Michigan State University, East Lansing, MI.

[31] Zeinali-Davarani, S., Raguin, L. G., Vorp, D. A., and Baek, S., 2011, "Identification of In Vivo Material and Geometric Parameters of a Human Aorta: Toward Patient-Specific Modeling of Abdominal Aortic Aneurysm," Biomech. Model. Mechanobiol., **10**(5), pp. 689–699.

[32] Humphrey, J. D., and Holzapfel, G. A., 2012, "Mechanics, Mechanobiology, and Modeling of Human Abdominal Aorta and Aneurysms," J. Biomech., **45**(5), pp. 805–814.

[33] Di Achille, P., Celi, S., Di Puccio, F., and Forte, P., 2011, "Anisotropic AAA: Computational Comparison Between Four and Two Fiber Family Material Models," J. Biomech., **44**(13), pp. 2418–2426.

[34] Martufi, G., Auer, M., Roy, J., Swedenborg, J., Sakalihasan, N., Panuccio, G., and Gasser, T. C., 2013, "Multidimensional Growth Measurements of Abdominal Aortic Aneurysms," J. Vasc. Surg., **58**(3), pp. 748–755.

[35] Wriggers, P., 2006, *Computational Contact Mechanics*, 2nd ed., Springer, The Netherlands.

[36] Doyle, B. J., Callanan, A., Burke, P. E., Grace, P. A., Walsh, M. T., Vorp, D. A., and McGloughlin, T. M., 2009, "Vessel Asymmetry as an Additional Diagnostic Tool in the Assessment of Abdominal Aortic Aneurysms," J. Vasc. Surg., **49**(2), pp. 443–454.

[37] Rissland, P., Alemu, Y., Einav, S., Ricotta, J., and Bluestein, D., 2009, "Abdominal Aortic Aneurysm Risk of Rupture: Patient-Specific FSI Simulations Using Anisotropic Model," ASME J. Biomech. Eng., **131**(3), p. 031001.

[38] Rodrguez, J. F., Ruiz, C., Doblaré, M., and Holzapfel, G. A., 2008, "Mechanical Stresses in Abdominal Aortic Aneurysms: Influence of Diameter, Asymmetry, and Material Anisotropy," ASME J. Biomech. Eng., **130**(2), p. 021023.

[39] Raghavan, M. L., Vorp, D. A., Federle, M. P., Makaroun, M. S., and Webster, M. W., 2000, "Wall Stress Distribution on Three-Dimensionally Reconstructed Models of Human Abdominal Aortic Aneurysm," J. Vasc. Surg., **31**(4), pp. 760–769.

[40] Xenos, M., Rambhia, S. H., Alemu, Y., Einav, S., Labropoulos, N., Tassiopoulos, A., Ricotta, J. J., and Bluestein, D., 2010, "Patient-Based Abdominal Aortic Aneurysm Rupture Risk Prediction With Fluid Structure Interaction Modeling," Ann. Biomed. Eng., **38**(11), pp. 3323–3337.

[41] Ruiz, D. S. M., Yilmaz, H., Dehdashti, A. R., Alimenti, A., Tribolet, N., and Rüfenacht, D. A., 2006, "The Perianeurysmal Environment: Influence on Saccular Aneurysm Shape and Rupture," Am. J. Neuroradiol., **27**(3), pp. 504–512.

[42] Sugiu, K., Jean, B., Ruiz, D. S. M., Martin, J. B., Delavelle, J., and Rüfenacht, D. A., 2000, "Influence of the Perianeurysmal Environment on Rupture of Cerebral Aneurysms. Preliminary Observation," Interventional Neuroradiol., **6**(Suppl. 1), pp. 65–70.

[43] Humphrey, J. D., and Na, S., 2002, "Elastodynamics and Arterial Wall Stress," Ann. Biomed. Eng., **30**(4), pp. 509–523.

[44] Liu, Y., Zhang, W., and Kassab, G. S., 2008, "Effects of Myocardial Constraint on the Passive Mechanical Behaviors of the Coronary Vessel Wall," Am. J. Physiol.: Heart Circ. Physiol., **294**(1), pp. H514–H523.

[45] Steelman, S. M., Wu, Q., Wagner, H. P., Yeh, A. T., and Humphrey, J. D., 2010, "Perivascular Tethering Modulates the Geometry and Biomechanics of Cerebral Arterioles," J. Biomech., **43**(14), pp. 2717–2721.

[46] Kim, J., Peruski, B. K., Hunley, S. C., Kwon, S. T., and Baek, S., 2013, "Influence of Surrounding Tissues on Biomechanics of Aortic Wall," Int. J. Exp. Comput. Biomech., **2**(2), pp. 105–117.

[47] Gharahi, H., Zambrano, B., Lim, C., Choi, J., Lee, W., and Baek, S., 2015, "On Growth Measurements of Abdominal Aortic Aneurysms Using Maximally Inscribed Spheres," Med. Eng. Phys., **37**(7), pp. 683–691.

[48] Vernerey, F., and Farsad, M., 2011, "A Constrained Mixture Approach to Mechano-Sensing and Force Generation in Contractile Cells," J. Mech. Behav. Biomed. Mater., **4**(8), pp. 1683–1699.

[49] Lopez-Candales, A., Holmes, D. R., Liao, S., Scott, M. J., Wickline, S. A., and Thompson, R. W., 1997, "Decreased Vascular Smooth Muscle Cell Density in Medial Degeneration of Human Abdominal Aortic Aneurysms," Am. J. Pathol., **150**(3), pp. 993–1007.

[50] Vande Geest, J. P., Wang, D. H. J., Wisniewski, S. R., Makaroun, M. S., and Vorp, D. A., 2006, "Towards a Noninvasive Method for Determination of Patient-Specific Wall Strength Distribution in Abdominal Aortic Aneurysms," Ann. Biomed. Eng., **34**(7), pp. 1098–1106.

[51] Di Martino, E. S., Bohra, A., Vande Geest, J. P., Gupta, N., Makaroun, M. S., and Vorp, D. A., 2006, "Biomechanical Properties of Ruptured Versus

Downloaded From: http://biomechanical.asmedigitalcollection.asme.org/ on 07/30/2015 Terms of Use: http://www.asme.org/about-asme/terms-of-use

Electively Repaired Abdominal Aortic Aneurysm Wall Tissue," J. Vasc. Surg., **43**(3), pp. 570–576.
[52] Veldenz, H. C., Schwarcz, T. H., Endean, E. D., Pilcher, D. B., Dorbin, P. B., and Hyde, G. L., 1994, "Morphology Predicts Rapid Growth of Small Abdominal Aortic Aneurysms," Ann. Vasc. Surg., **8**(1), pp. 10–13.
[53] Sacks, M. S., Vorp, D. A., Raghavan, M. L., Federle, M. P., and Webster, M. W., 1999, "In Vivo Three-Dimensional Surface Geometry of Abdominal Aortic Aneurysms," Ann. Biomed. Eng., **27**(4), pp. 469–479.
[54] Giannoglou, G., Giannakoulas, G., Soulis, J., Chatzizisis, Y., Perdikides, T., Melas, N., Parcharidis, G., and Louridas, G., 2006, "Predicting the Risk of Rupture of Abdominal Aortic Aneurysms by Utilizing Various Geometrical Parameters: Revisiting the Diameter Criterion," Angiology, **57**(4), pp. 487–494.
[55] Doyle, B. J., Cloonan, A. J., Walsh, M. T., Vorp, D. A., and McGloughlin, T. M., 2010, "Identification of Rupture Locations in Patient-Specific Abdominal Aortic Aneurysms Using Experimental and Computational Techniques," J. Biomech., **43**(7), pp. 1408–1416.
[56] Raghavan, M. L., and Vorp, D. A., 2000, "Toward a Biomechanical Tool to Evaluate Rupture Potential of Abdominal Aortic Aneurysm: Identification of a Finite Strain Constitutive Model and Evaluation of Its Applicability," J. Biomech., **33**(4), pp. 475–482.
[57] Vorp, D. A., and Vande Geest, J. P., 2005, "Biomechanical Determinants of Abdominal Aortic Aneurysm Rupture," Arterioscler., Thromb., Vasc. Biol., **25**(8), pp. 1558–1566.
[58] Xenos, M., Rambhia, S., Alemu, Y., Einav, S., Ricotta, J. J., Labropoulos, N., Tassiopoulos, A., and Bluestein, D., 2010, "Patient Based Abdominal Aortic Aneurysm Rupture Risk Prediction Combining Clinical Visualizing Modalities With Fluid Structure Interaction Numerical Simulations," 32nd Annual International Conference of the IEEE EMBS Buenos Aires.
[59] Seyedsalehi, S., Zhang, L., Choi, J., and Baek, S., "Prior Distribution of Material Parameters for a Computational Model of the Abdominal Aorta," ASME J. Biomech. Eng. (to be published).
[60] Farsad, M., Zambrano, B., and Baek, S., 2015, "Data-Guided Growth and Remodeling Model of Abdominal Aortic Aneurysm Accounting for the Bio-Chemical Effects of Intraluminal Thrombus," *Computational Biomechanics for Medicine, New Approaches and New Applications*, Springer International Publishing, pp. 13–23.

Downloaded From: http://biomechanical.asmedigitalcollection.asme.org/ on 07/30/2015 Terms of Use: http://www.asme.org/about-asme/terms-of-use